Molecularly thin two-dimensional hybrid perovskites with tunable optoelectronic properties due to reversible surface relaxation

Kai Leng [1,2,3,7], Ibrahim Abdelwahab[1,3,4,7], Ivan Verzhbitskiy [3,5], Mykola Telychko[1,3], Leiqiang Chu [1,3], Wei Fu[1,3], Xiao Chi[1], Na Guo[5], Zhihui Chen[1], Zhongxin Chen[1,4], Chun Zhang [5], Qing-Hua Xu[1], Jiong Lu[1,3], Manish Chhowalla[6], Goki Eda [1,3,5] and Kian Ping Loh [1,2,3]*

Due to their layered structure, two-dimensional Ruddlesden–Popper perovskites (RPPs), composed of multiple organic/inorganic quantum wells, can in principle be exfoliated down to few and single layers. These molecularly thin layers are expected to present unique properties with respect to the bulk counterpart, due to increased lattice deformations caused by interface strain. Here, we have synthesized centimetre-sized, pure-phase single-crystal RPP perovskites $(CH_3(CH_2)_3NH_3)_2(CH_3NH_3)_{n-1}Pb_nI_{3n+1}$ ($n = 1$–4) from which single quantum well layers have been exfoliated. We observed a reversible shift in excitonic energies induced by laser annealing on exfoliated layers encapsulated by hexagonal boron nitride. Moreover, a highly efficient photodetector was fabricated using a molecularly thin $n = 4$ RPP crystal, showing a photogain of 10^5 and an internal quantum efficiency of ~34%. Our results suggest that, thanks to their dynamic structure, atomically thin perovskites enable an additional degree of control for the bandgap engineering of these materials

Organic–inorganic layered perovskites are quantum hybrid materials possessing the physical properties of both organic semiconductors and inorganic semiconducting quantum wells[1]. Ruddlesden–Popper perovskites (RPPs)[2] are archetypical examples of this class of layered materials; they have the general formula $(RNH_3)_2(CH_3NH_3)_{n-1}Pb_nX_{3n+1}$, where R is an alkyl or aromatic group and X is the halide. Researchers in the last two decades have studied the RPP perovskites and its higher homologues to understand how their physical properties scale with the thickness of the quantum well; that is $n = 4$ crystal has a thicker quantum well than $n = 1$ (refs [3–9]). In particular, quasi-two-dimensional perovskites containing mixed phases with different bandgaps have been synthesized, and excitonic energy transfer among these phases has led to improvement in optoelectronic performance[10,11].

A potentially rich area to explore is the molecular analogue of graphene in these layered RPP crystals when they are scaled to molecular thickness or single unit cell (that is, single quantum well) dimensions[12,13]. Unlike the structurally rigid inorganic semiconductor quantum well, hybrid two-dimensional (2D) perovskite is maintained by a combination of ionic and hydrogen bonds, rendering it molecularly soft and easy to delaminate (Supplementary Fig. 1). In principle, reducing 2D perovskites to the thickness of a single quantum well should further lower their deformation energy, thereby making them good candidates for strain engineering. At the mono-unit cell level, surface relaxation of the organic cations may lead to cooperative lattice distortion, resulting in varied electronic structure[14]. With the aim of investigating whether the properties of 2D perovskites are unique at the molecularly thin limit, we synthesized centimetre-sized crystals grown by a temperature-programmed crystallization method[15], from which large-sized monolayer perovskite (defined here as mono-unit cell thickness) sheet can be exfoliated. Without employing the ultrahigh-pressure methods used by researchers to induce lattice compression[16–18], we discover that laser-induced surface relaxation can be used to modulate the energy landscapes in molecularly thin RPP perovskites in a highly reversible way, leading to reversible excitonic states. By studying the photoresponsivity of the single-crystal perovskites as a function of thickness, we further discover tunnelling of carriers or excitons across the hybrid interlayers, leading to efficient photocurrent generation.

Structural and optical properties of RPP single crystals
To study the fundamental properties of 2D RPP monolayers across the homologous series, we synthesized large-sized crystals of $(CH_3(CH_2)_3NH_3)_2(CH_3NH_3)_{n-1}Pb_nI_{3n+1}$ ($n = 1, 2, 3, 4$) using a temperature-programmed crystallization method (Fig. 1a–d). The phase purity of the as-grown large-sized RPP ($n = 1$–4) crystals was confirmed by X-ray diffraction (XRD) (Supplementary Fig. 2 and Supplementary Tables 1 and 2)[2] and optical absorption studies to be single phase (Fig. 2a). The centimetre-sized RPP single crystals can be exfoliated to yield monolayer flakes with lateral dimensions between 20 and 100 μm, as shown in Fig. 1i–l and Supplementary Fig. 3. The corresponding height profiles obtained by atomic force microscopy (AFM) indicate that the thicknesses of the monolayers with varying n values agree reasonably well with the c-axis lattice constants (Fig. 1e–h) of mono-unit cell 2D RPPs. The optical properties of both bulk and monolayer flakes were investigated by photoluminescence and optical absorption measurements. As shown in Fig. 2a,

[1]Department of Chemistry, National University of Singapore, Singapore, Singapore. [2]Solar Energy Research Institute of Singapore (SERIS), Singapore, Singapore. [3]Center for Advanced 2D Materials and Graphene Research Centre, Singapore, Singapore. [4]NUS Graduate School for Integrative Sciences and Engineering, National University of Singapore, Singapore, Singapore. [5]Department of Physics, National University of Singapore, Singapore, Singapore. [6]Materials Science and Engineering, Rutgers University, Piscataway, NJ, USA. [7]These authors contributed equally: Kai Leng, Ibrahim Abdelwahab.
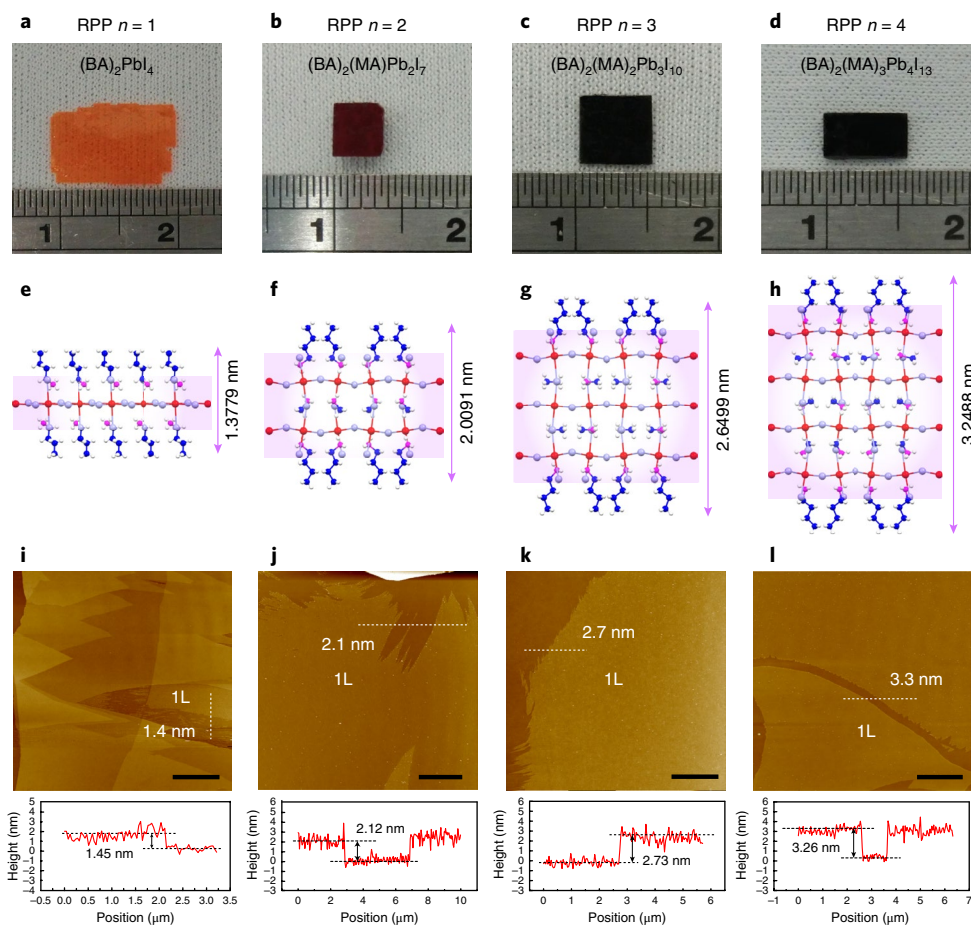*e-mail: chmlohkp@nus.edu.sg

Fig. 1 | Large-sized monolayers (n = 1, 2, 3, 4 series) mechanically exfoliated from bulk (CH₃(CH₂)₃NH₃)₂(CH₃NH₃)ₙ₋₁PbₙI₃ₙ₊₁ single crystals. a–d, Photographs of centimetre-sized RPP single crystals with n from 1 to 4. **e–h**, Schematic showing a side view of the monolayer series (n varies from 1 to 4) along with their c-axis lattice constants. Different colours represent different elements: red, Pb; violet, I; blue, C; pink, N; white, H. **i–l**, AFM images and corresponding height profiles along the dotted line in the images of the monolayer (1L) RPP series (n = 1 to 4). Scale bars, 4 μm (**i–l**).

from $n = 1$ to 4 homologues, the photoluminescence of both bulk and monolayer flakes is found to shift progressively towards longer wavelengths in accordance with their decreasing bandgap. It is also obvious that the photoluminescence peaks of the exfoliated molecularly thin flakes are much sharper than those for bulk crystals. The narrow-linewidth photoluminescence peaks of the monolayer RPP flakes with small Stokes shifts (Fig. 2b–e) compared to bulk crystals attest to their highly crystalline quality, because the presence of defects will increase the Stokes shift due to non-radiative recombination.

Reversible order–disorder transition in RPP monolayers

The exfoliated flakes were found to be much more reactive than the bulk crystals and decomposed rapidly under laser irradiation in air (Supplementary Fig. 4). An effective way to prevent photo-induced degradation is to encapsulate the exfoliated flake with a hexagonal boron nitride (hBN) layer (this is impermeable to almost all gases and is optically transparent[19,20]; Fig. 3a,b). All the photoluminescence studies described hereafter were subsequently carried out with the exfoliated perovskite flake protected by the hBN flake. Beginning from the initial state where the photoluminescence peaks were sharp and originate from single excitonic state, a longer time exposure to the laser used for photoluminescence study was found to induce a redshift and broaden the photoluminescence. Figure 3c presents a representative photoluminescence spectral evolution for the $n = 2$ RPP monolayer, in which the initially sharp photoluminescence peak (stage I) broadens progressively with laser irradiation

time (stage II), and eventually becomes less broad (stage III) when it reached a final redshifted state. Similar spectral evolution can be observed for other n value members, although the extent of the redshift window reduces as n increases (Fig. 3h). Interestingly, the entire photoluminescence evolution can be reversed if the sample is subjected to a higher power laser annealing under vacuum, where it goes from stage III back to stage I (Fig. 3d). The photoluminescence redshift and its reversal can be thermally activated over tens of cycles by performing laser annealing (Fig. 3e), indicating that any defects that are created are dynamic in nature and can be annealed out. We propose that the reversible spectral evolution is due to a dynamic equilibrium involving structural reorientation of the organic chains in the easily deformed 2D perovskite flakes, in which the hBN protection layer plays the important role of confining the organic cations and preventing their escape, thereby increasing their probability of returning to the lattice following a laser annealing process. Figure 3f presents a photoluminescence colour map under a continuous-wave laser excitation power of 5.21 μW (532 nm), where the reversible spectral shift can be seen for two cycles, suggesting that the relaxation and derelaxation process are in dynamic equilibrium. The order–disorder transition process we observe here may be analogous to the crystal regrowth process in bulk 3D perovskite crystal following post-annealing, except that the regrowth process is limited to the surface here.

Thermal fluctuations caused by laser annealing increase the orientation disorder of the surface organic cations in the molecular thin flakes, so it is likely that trap states are created[21]. Bound excitons
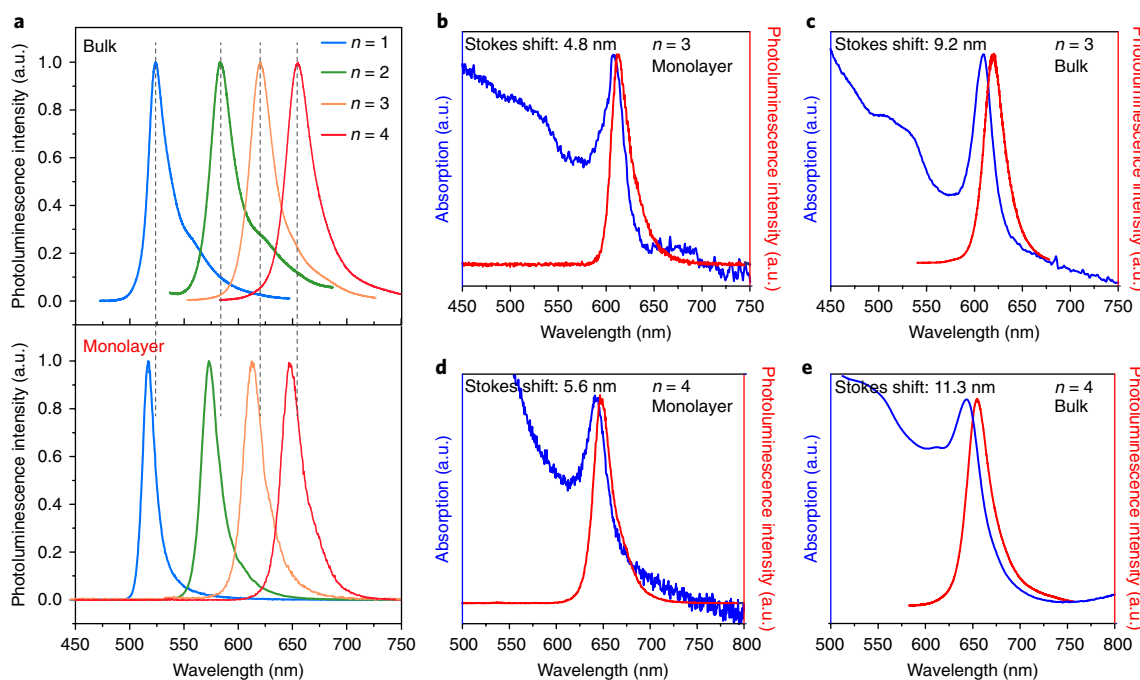
Fig. 2 | Optical characterization of bulk and monolayer (single unit cell) RPP flakes. a, Photoluminescence of exfoliated monolayer (bottom) versus bulk crystals (top) for RPP of $n = 1$ to 4 homologues. **b–e**, Comparison of the difference in absorption maxima and photoluminescence (Stokes shift) for $n = 3$ and $n = 4$ monolayer and bulk flakes.

can be formed when free excitons become localized at these traps. Due to the high oscillator strengths of the bound exciton[22], strong photoluminescence can be obtained, as opposed to the quenched photoluminescence intensity seen in decomposed crystal. A temperature-dependent photoluminescence study was performed to interrogate the change in the relative intensity of the band-edge exciton peak and the redshifted peak in the photoluminescence spectrum. For the sake of subsequent discussion, we define the state with the redshifted photoluminescence as the 'relaxed' state, to denote the situation where the monolayer perovskite has been restructured by laser annealing, versus the 'derelaxed' state where the photoluminescence arises from the near band-edge exciton (original position). It is noticed that the intensities of both derelaxed- and relaxed-state photoluminescence peaks increase sharply when the temperature is lowered, but the ratio $I_{relax}/I_{derelax}$ increases much more sharply with decreasing temperature (Fig. 3g). This agrees well with the relaxed state being assigned to bound excitons, which are more efficient emitters than free excitons at low temperatures; the thermalization of bound exciton to free exciton at higher temperature reduces luminescence intensity.

The surface relaxation effects are observed to be more pronounced in monolayers than in thicker layers, as judged from the larger magnitude of photoluminescence redshifts in the former; this can be explained by the bulk dilution effects in thicker samples. For example a thickness dependence for the magnitude of the photoluminescence redshift is observed for $n = 1$–4 RPP (Fig. 3h), where the $n = 4$ monolayer RPP flake shows the smallest redshift among the homologues studied due to its thickest inorganic quantum well. Supplementary Fig. 5a-d shows the photoluminescence of $n = 2$ RPP flakes of different layer thicknesses ranging from monolayer to quadruple-layer, indicating that the redshift window becomes increasingly smaller when the thickness of the crystal increases. A similar trend of decreasing redshift window with increased layer thickness is also displayed by $n = 3$ and $n = 4$ RPP flakes (Supplementary Figs. 5e–g and Fig. 6).

To obtain direct visual evidence of structural relaxation, we used a Q-plus non-contact atomic force microscope (nc-AFM) to probe

the relaxation of the organic chains when the exfoliated perovskite flake was subjected to thermal stress, simulating the thermal annealing effects by laser irradiation. nc-AFM directly interrogates the n-butyl ammonium organic chains and tracks their in-plane and out-of-plane relaxation when thermally stressed. In situ exfoliation was performed in ultrahigh vacuum to observe the as-exfoliated structure of the surface. High-resolution topography nc-AFM images reveal that the as-exfoliated perovskite surface initially consists of a highly ordered periodic square lattice with a low density of vacancies and defects ($<1 \times 10^{11}\,\text{cm}^{-2}$). The unit cell has lattice constants of 8.73 Å × 8.88 Å, as indicated in Fig. 4a, which is slightly contracted by 7.9–9.5% with respect to the bulk values determined by XRD. On annealing to 45 °C, we observed that vacancies start to appear (Fig. 4b and Supplementary Fig. 7). More importantly, by prolonging the annealing time or increasing the temperature, we obtained direct visual evidence of the reorientation of the surface organic cations, in which a new zigzag assembly (relaxed state, Fig. 4c,d) emerged and coexisted with the square lattice (derelaxed state). As shown in Fig. 4e, the zigzag assembly shows a vertical displacement of about +20 pm height (profile 1) relative to the square lattice height (profile 2) in the out-of-plane view, and coverage of their domains increases on annealing at higher temperature. The zigzag and square lattice assembly are also interconvertible by using the tip to apply pressure on the surface (Supplementary Fig. 8). By changing the frequency shift (df) setpoint and consequently the tip–sample separation, we can induce a conversion from the square lattice to zigzag lattice and vice versa due to tip-induced out-of-plane tilting of the surface chains. This observation is indicative of the molecular softness of the surface organic cations and its easily deformable nature.

The reorientations of these organic chains as well as the generation of vacancies affect the optical properties and translate into the redshifts of photoluminescence observed in this work. As shown in Fig. 4f, by using in situ valence band spectroscopy, we observed that these relaxations increased the intensity of the density of states (DOS) near the Fermi level; this indicates that trap states may be created, which can suppress the rate of recombination by trapping
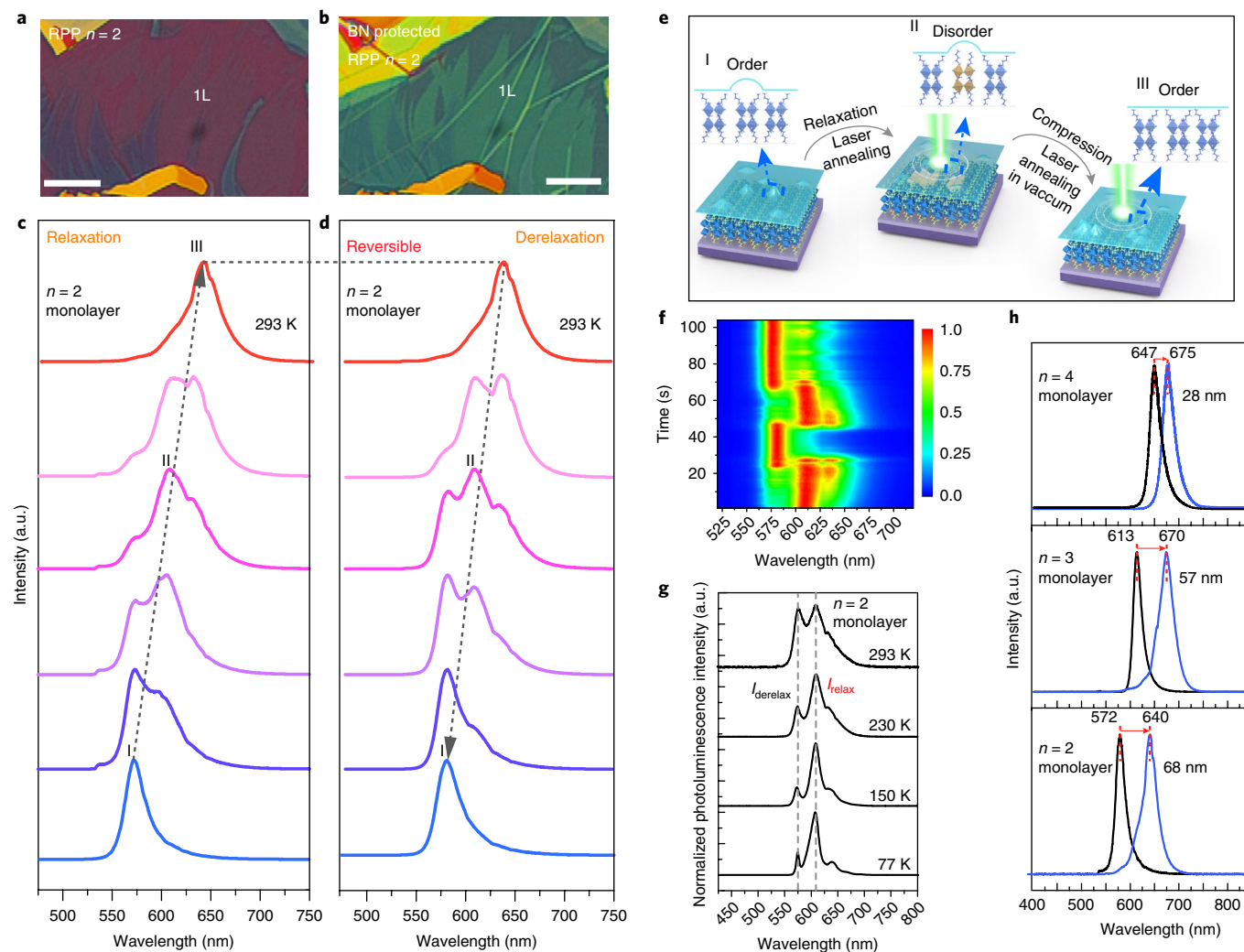
Fig. 3 | Reversible exciton states in RPP monolayers. a,b, Optical image of monolayer (1L) RPP $n = 2$ flake on Si/SiO$_2$ (**a**) and after hBN encapsulation (**b**). Scale bars (**a,b**), 20 μm. **c**, Redshift of photoluminescence in RPP $n = 2$ monolayer from a near band-edge exciton state at 572 nm to 640 nm, due to surface relaxation. **d**, Corresponding derelaxation process in which the photoluminescence blueshifts from the relaxed state at 640 nm to the near band-edge exciton state. **e**, Schematic diagram showing the order–disorder transition by laser illumination. **f**, Photoluminescence colour map showing two continuous cycles of photoluminescence shifts during order–disorder transition, plotted as a function of laser irradiation time, emission wavelength and intensity. **g**, Temperature-dependent changes in photoluminescence intensity, highlighting changes in the relative intensity of I_{relax} and $I_{derelax}$ of monolayer $n = 2$ RPP flake. **h**, Photoluminescence of $n = 2$–4 RPP monolayers. Black lines indicate initial state photoluminescence and blue lines are photoluminescence after relaxation; the spectral shift window decreases as n increases due to the increasing thickness of the quantum well.

one particular type of charge carrier, increasing the photogain. Hole traps existing in a 3D perovskite film top surface have been reported to contribute to a high gain in these devices[23].

Insights into the changes in the DOS of the perovskite monolayer as a result of surface relaxation and the formation of organic cation vacancies can be obtained by performing first-principles calculations with density functional theory (DFT), utilizing the Vienna ab initio simulation package (VASP)[24]. Due to the size of the unit cells, we only performed calculations for $n = 1$ and 2. The bandgaps are underestimated in these calculations but the trend is instructive. Mirroring the trend seen in experiments, the simulation results show that the presence of organic cation vacancies causes the valence band-edge to move towards the Fermi level, and narrows the gap. The creation of a second organic cation vacancy will further reduce the bandgap (Supplementary Fig. 9). It should be pointed out that in our experiments, confinement by the hBN layer on the perovskites prevents misplaced organic cations from desorbing, and these defects can be thermally cured.

Photodetectors based on monolayer and bulk RPP flakes

In terms of photocurrent conversion efficiency, molecularly thin 2D perovskites in principle allow a more effective extraction of carriers and better electrostatic control compared to bulk crystal. In addition, the presence of any vacancies or surface deformation will exert a strong effect on the electronic properties of such molecularly thin layers. Shallow trap states can contribute to photogain in a photodetector, for example by trapping the holes and allowing the electrons to circulate longer. In the dynamically disordered energy landscape induced by laser annealing, another effect that can be convoluted with the presence of trap states is the self-doping effect due to the generation of organic cation vacancies. To investigate this, we fabricated a photodetector made from monolayer and bilayer flakes of 2D perovskites ($n = 4$) by dry transfer; these were electrically contacted by bottom gold contacts formed by electron-beam lithography on thermally grown silicon dioxide. The source–drain channel was 1 μm long, and the device was capped by hBN (Fig. 5a and Fig. 5b, inset). The photocurrents in these devices are highly robust
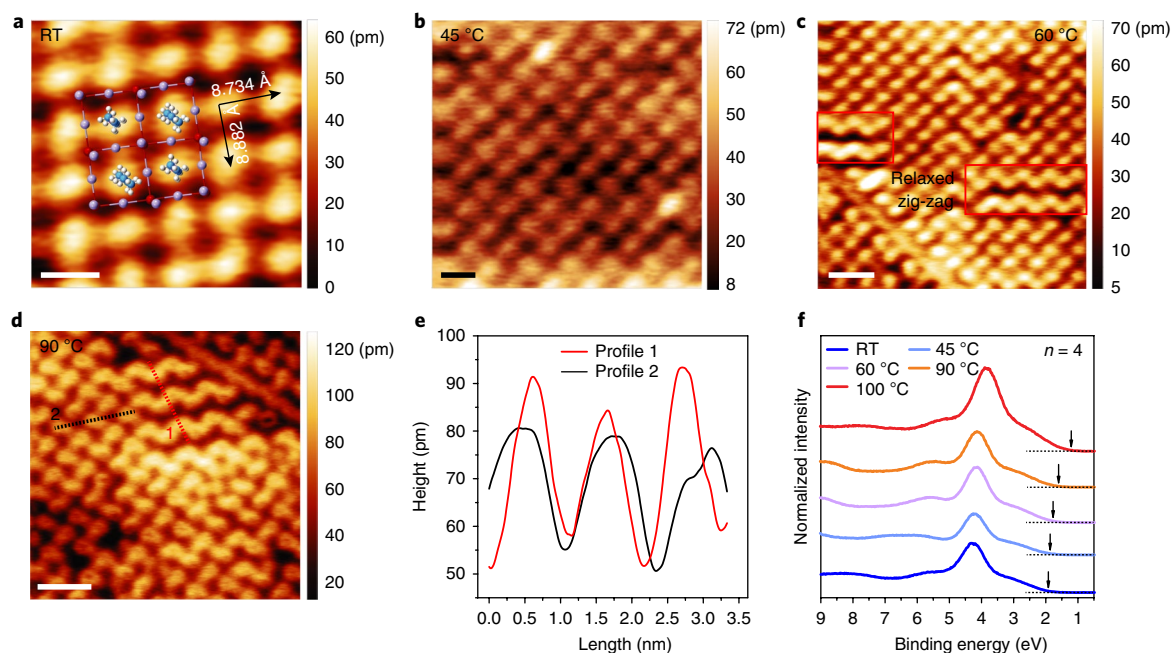
Fig. 4 | Q-plus nc-AFM images on in situ exfoliated $n = 4$ RPP flake surface. a, Initial state of the surface consists of square lattice. The overlapped sketch displays a suggested top view structure of four unit cells of the $n = 4$ RPP. The bright dot in the image originates from the organic cation, drawn as a tilted four-carbon chain, while the inorganic part is deeper and is not imaged. RT, room temperature. Scale bar, 1 nm. **b–d,** The sample was thermally annealed to 45 °C (**b**), 60 °C (**c**) and 90 °C (**d**). It can be seen that zigzag (relaxed) states emerge and become the dominant surface features; this is paralleled by the appearance of vacancies after a higher temperature annealing. Scale bars, 1 nm (**b**), 2 nm (**c**), 2 nm (**d**). **e,** Height measurements along the red (profile 1) and black (profile 2) dotted lines in **d**, where the zigzag lattice corrugations show about +20 pm vertical displacement compared to the square lattice corrugations. **f,** In situ valence band spectroscopy tracking the changes in DOS near the valence band-edge.

and increase linearly with laser power. The relaxed and derelaxed states can be reversibly and precisely controlled in one device by laser annealing and substrate cooling processes. Simultaneous photoluminescence measurement was used to distinguish derelaxed state (~650 nm photoluminescence) from relaxed state (~675 nm photoluminescence) of the $n = 4$ perovskite photodetector. As shown in Fig. 5b, the current–voltage (I_{SD}–V_{SD}) curves of relaxed and derelaxed states were collected at 77 K under 1.71 μW and 0.28 μW laser power, respectively. From the I–V curves, the photo-current from the relaxed state is approximately three times higher than that of the derelaxed state at the same power. Importantly, the incident photocurrent efficiency (IPCE) spectra of the relaxed state in Fig. 5c shows a second photocurrent peak at 653 nm, which is redshifted from the initial band-edge exciton at 640 nm, thereby indicating that the relaxed state is absorptive in nature, through which photocurrents can be generated with high efficiency. In Fig. 5c, the photoluminescence peaks are plotted together with the IPCE spectra, showing the excitonic redshift that parallels the redshifted photocurrent peak.

The I–V curves of the monolayer (relaxed state), bulk and bilayer (relaxed state) $n = 4$ perovskite photodetectors under focused laser illumination are presented in Fig. 5d,e and Supplementary Fig. 10h. All I–V curves show ohmic conduction under illumination and display ultralow dark current (10^{-13} A). The absorbance of monolayer and bulk flakes on quartz substrates was derived from transmittance measurements, from which the internal quantum efficiency (IQE) can be calculated (Supplementary Fig. 10a–g). Monolayer $n = 4$ RPP was determined to absorb 8% light at 532 nm. When fabricated into a photodetector and excited with a laser, the current reached 610 nA at a laser excitation power of 346 μW when the source–drain voltage was 3 V (Fig. 5d), which is more than five orders of magnitude higher than the dark current. Because of the extremely low dark current, which is key to the reliability of the photodetector, our 2D

perovskite photodetectors exhibit good figures of merit based on the different thickness of the perovskite flakes. As shown in Fig. 5f, the calculated photodetectivities D^* were to be 4.7×10^{10} Jones for the monolayer, increasing to 1.1×10^{12} Jones for bulk perovskite flakes excited by a focused laser beam. Under focused laser with 532 nm excitation (1 μm² spot area) illumination conditions we calculated the photoresponsivity values to be 11.3, 24.2 and 71.9 mA W⁻¹ at an excitation laser power of 36 nW for the monolayer, bilayer and bulk perovskites, respectively. To gain further insight into the photometrics of our perovskites, we performed measurements under defocused laser illumination, which provides lower light power densities compared to a focused beam. Our bulk perovskite photodetector with flake thickness around 20 nm exhibits a 7.4×10^4 A W⁻¹ responsivity with an ultrahigh photodetectivity of 1.2×10^{15} under a defocus laser illumination with a wavelength of 532 nm (see description of calculations in the Methods and Supplementary Fig. 10j). These metrics are better than for a non-gated, pristine monolayer transition-metal dichalcogenide photodetector structure in the absence of heterostructure-assisted charge separation[25] or a ferroelectric polymer-induced internal electric field[26]. The increase in photocurrent for thicker flakes (Fig. 5e) compared to the monolayer affirms that photocurrent is limited by the density of sensitivity states, and that excitons are able to tunnel across the layers to be dissociated at electrodes. The IQE values for the monolayer and bilayer were calculated to be 34% and 44%, respectively (Fig. 5f and calculations in the Methods); such a high IQE value is indeed surprising in view of the large exciton binding energies of 2D RPP, which are commonly thought to discourage exciton dissociation. We attribute the high photocurrent yield to the high photoconductive gain of the perovskite device due to the presence of shallow trap states as well as the self-doping effect induced by organic cation vacancies[27]. Carrier lifetime measurements carried out using time-resolved photoluminescence confirmed that the carrier lifetime was
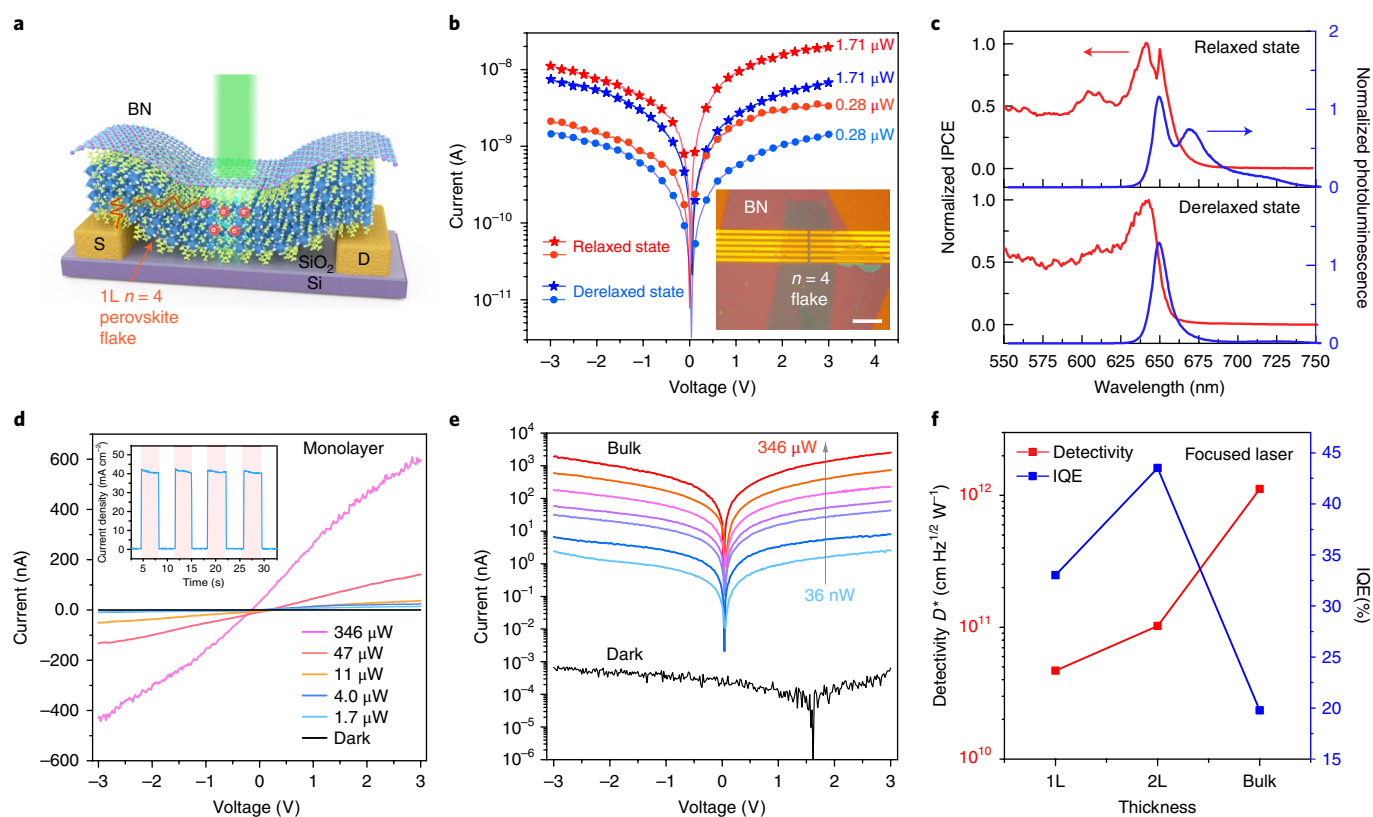
Fig. 5 | ($C_4H_9NH_3$)$_2$(CH_3NH_3)$_3$Pb$_4$I$_{13}$ $n=4$ perovskite photodetector device fabricated on exfoliated flakes of different thickness, with excitation by a 532 nm focused laser of spot size 1 μm². **a**, Schematic of photodetector device structure of monolayer $n=4$ RPP flake where charge collection is by bottom electrode. **b**, Current–voltage (I_{SD}–V_{SD}) curves of relaxed and derelaxed states under two incident laser powers. Inset, Optical image of a typical monolayer thickness device. Source–drain channel length is 1 μm. Scale bar, 20 μm. **c**, Red line, IPCE of relaxed and derelaxed state in $n=4$ RPP monolayer flakes. Blue line, Corresponding photoluminescence. **d**, I–V characteristics of monolayer $n=4$ RPP device tested in the relaxed state in the dark and under increasing power density. Inset, On–off photocurrent response of the monolayer $n=4$ RPP device. **e**, I–V curves of the bulk device in the dark and under different illumination intensities. **f**, Comparison of detectivity D^* and IQE performance of a photodetector device made from monolayer, bilayer and bulk RPP flakes.

longer for the relaxed state compared to the derelaxed states, which supports the fact that carrier recombination is suppressed in the relaxed state, thus facilitating escape of carriers into the electrodes (Supplementary Fig. 11). The role of hBN as a protection layer is important. We observed that increased laser irradiation time or power of the unprotected perovskite sample will lead to a higher defect concentration and thus create more recombination centres (hence shorter carrier lifetime), but the situation is different in the case of hBN-protected flakes due to the ability of the defects to be repaired by further laser annealing, thus limiting the concentration of defects in the relaxed state. The photoconductive gain of the $n=4$ RPP crystal is calculated to be 1.7×10^5 under defocused laser illumination (calculations in the Methods), and such a high photogain value is comparable to that for a solution-processed 3D perovskites photodetector interfaced to a hole blocking layer[23].

Outlook

In conclusion, molecularly thin perovskites display optical properties that are different from their bulk counterparts due to their easily deformable nature and surface relaxation effects. Confining the surface of ultrathin (<6 nm thickness) RPP perovskites with hBN allows dynamic surface relaxation to be activated by thermal energy without introducing permanent defects. The RPP perovskite photodetector has extremely low dark current due to a highly resistive state in the dark, while a highly conductive state is switched on under illumination with photocarriers or excitons that can tunnel across the interlayers, contributing to a high responsivity and detectivity value. The ability to induce reversible excitonic transitions

at a confined interface allows bandgap engineering of molecularly thin perovskites. One way to exploit the surface relaxation effect is through interface engineering of these 2D perovskites and other 2D materials, whereby strain-tuning of coupling at the interface can lead to advanced hybrid materials with novel properties.

Online content

Any methods, additional references, Nature Research reporting summaries, source data, statements of data availability and associated accession codes are available at https://doi.org/10.1038/s41563-018-0164-8.

References

1. Novoselov, K., Mishchenko, A., Carvalho, A. & Neto, A. C. 2D materials and van der Waals heterostructures. *Science* **353**, aac9439 (2016).
2. Stoumpos, C. C. et al. Ruddlesden–Popper hybrid lead iodide perovskite 2D homologous semiconductors. *Chem. Mater.* **28**, 2852–2867 (2016).
3. Mitzi, D. B., Feild, C. A., Harrison, W. T. A. & Guloy, A. M. Conducting tin halides with a layered organic-based perovskite structure. *Nature* **369**, 467–469 (1994).
4. Ishihara, T., Takahashi, J. & Goto, T. Optical properties due to electronic transitions in two-dimensional semiconductors ($C_nH_{2n+1}NH_3$)PbI$_4$. *Phys. Rev. B* **42**, 11099–11107 (1990).
5. Tanaka, K. et al. Electronic and excitonic structures of inorganic-organic perovskite-type quantum-well crystal ($C_4H_9NH_3$)$_2$PbBr$_4$. *Jpn J. Appl. Phys.* **44**, 5923–5932 (2005).
6. Saparov, B. & Mitzi, D. B. Organic–inorganic perovskites: structural versatility for functional materials design. *Chem. Rev.* **116**, 4558–4596 (2016).

7. Shi, E. et al. Two-dimensional halide perovskite nanomaterials and heterostructures. *Chem. Soc. Rev.* **47**, 6046–6072 (2018).

8. Tsai, H. et al. High-efficiency two-dimensional Ruddlesden–Popper perovskite solar cells. *Nature* **536**, 312–316 (2016).

9. Blancon, J.-C. et al. Extremely efficient internal exciton dissociation through edge states in layered 2D perovskites. *Science* **355**, 1288–1292 (2017).

10. Quan, L. N. et al. Tailoring the energy landscape in quasi-2D halide perovskites enables efficient green-light emission. *Nano Lett.* **17**, 3701–3709 (2017).

11. Yuan, M. J. et al. Perovskite energy funnels for efficient light-emitting diodes. *Nat. Nanotech.* **11**, 872–877 (2016).

12. Dou, L. et al. Atomically thin two-dimensional organic–inorganic hybrid perovskites. *Science* **349**, 1518–1521 (2015).

13. Niu, W., Eiden, A., Prakash, G. V. & Baumberg, J. Exfoliation of self-assembled 2D organic–inorganic perovskite semiconductors. *Appl. Phys. Lett.* **104**, 171111 (2014).

14. Yaffe, O. et al. Excitons in ultrathin organic–inorganic perovskite crystals. *Phys. Rev. B* **92**, 045414 (2015).

15. Mitzi, D. B. in *Progress in Inorganic Chemistry* Vol. 48 (ed. Karlin, K.) 1–121 (Wiley, New York, NY, 1999).

16. Jaffe, A. et al. High-pressure single-crystal structures of 3D lead-halide hybrid perovskites and pressure effects on their electronic and optical properties. *ACS Cent. Sci.* **2**, 201–209 (2016).

17. Kong, L. P. et al. Simultaneous band-gap narrowing and carrier-lifetime prolongation of organic–inorganic trihalide perovskites. *Proc. Natl Acad. Sci. USA* **113**, 8910–8915 (2016).

18. Xiao, G. J. et al. Pressure effects on structure and optical properties in cesium lead bromide perovskite nanocrystals. *J. Am. Chem. Soc.* **139**, 10087–10094 (2017).

19. Kubota, Y., Watanabe, K., Tsuda, O. & Taniguchi, T. Deep ultraviolet light-emitting hexagonal boron nitride synthesized at atmospheric pressure. *Science* **317**, 932–934 (2007).

20. Cheng, H.-C. et al. Van der Waals heterojunction devices based on organohalide perovskites and two-dimensional materials. *Nano. Lett.* **16**, 367–373 (2016).

21. Wu, X. X. et al. Trap states in lead iodide perovskites. *J. Am. Chem. Soc.* **135**, 2089–2096 (2015).

22. Stébé, B., Assaid, E., Le Goff, S. & Dujardin, F. Giant oscillator strengths of ionized donor bound excitons in semiconductor quantum crystallites. *Solid State Commun.* **100**, 217–220 (1996).

23. Dong, R. et al. High-gain and low-driving-voltage photodetectors based on organolead triiodide perovskties. *Adv. Mater.* **27**, 1912–1918 (2015).

24. Kresse, G. & Hafner, J. Ab initio molecular dynamics for liquid metals. *Phys. Rev. B* **47**, 558–561 (1993).

25. Yin, Z. Y. et al. Single-layer MoS_2 phototransistors. *ACS Nano* **6**, 74–80 (2012).

26. Wang, X. D. et al. Ultrasensitive and broadband MoS_2 photodetector driven by ferroelectrics. *Adv. Mater.* **27**, 6575–6581 (2015).

27. Furchi, M. M., Polyushkin, D. K., Pospischil, A. & Mueller, T. Mechanisms of photoconductivity in atomically thin MoS_2. *Nano. Lett.* **135**, 2089–2096 (2015).

Acknowledgements

Author contributions

K.L. and K.P.L. conceived and designed the experiments. K.L. fabricated all RPP single crystals. K.L. and I.A. prepared all atomically thin samples and performed AFM measurements in the glove box. I.V. and K.L. tested the PC device. M.T. performed Q-plus AFM scanning. K.L. and I.A. prepared samples for Q-plus nc-AFM scanning. K.L., L.Q.C. and I.A. performed photoluminescence measurements. I.A. and K.L. fabricated the devices. N.G. performed calculations. K.L. and K.P.L. wrote the manuscript. All authors contributed to the overall scientific interpretation.

Competing interests

The authors declare no competing interests.

Additional information

Supplementary information is available for this paper at https://doi.org/10.1038/s41563-018-0164-8.

Reprints and permissions information is available at www.nature.com/reprints.

Correspondence and requests for materials should be addressed to K.P.L.

Publisher's note: Springer Nature remains neutral with regard to jurisdictional claims in published maps and institutional affiliations.

Methods

2D lead RPP single crystals with the chemical formula $(CH_3(CH_2)_3NH_3)_2$ $(CH_3NH_3)_{n-1}Pb_nI_{3n+1}$ were synthesized using three solid precursors—PbO, $C_4H_9NH_3I$ (BAI) and CH_3NH_3I (MAI)—via a temperature-programmed solution precipitation method.

Synthesis of $C_4H_9NH_3I$. Butyl amine (10 ml, Aldrich, 99.5%) and 25 ml of iced methanol were added to a 250 ml round-bottom flask chilled at 0 °C. The mixture was then stirred for 5 min. Concentrated HI (10 ml, Aldrich, 57 wt% in water) was subsequently added dropwise to the cold mixture using a syringe needle. The mixture was allowed to stir at room temperature for an additional 2 h, then the solvent was removed with a rotary evaporator at 70 °C. The crude white solid product was washed with 3×30 ml of diethyl ether by stirring for 90 min, followed by decanting of the solvent. The washed product was then recrystallized using a chloroform/diethyl ether mixed solvent. After filtration, the snow-white powder crystal was dried in vacuum at 70 °C before storage in a glove box for subsequent use.

The reaction stoichiometry was carefully controlled to obtain pure iodide RPP crystals, especially for higher-n members.

$(BA)_2(MA)_3Pb_4I_{13}$ ($n = 4$). PbO (0.69 M), BAI (0.17 M) and MAI (0.52 M) precursors were dispersed in a concentrated HI and H_3PO_2 mixture (7.6:1, vol/vol) in an Ar-filled glove box, and then heated at 110 °C with stirring for 40 min to give a clear yellow solution. The solution was quickly transferred to an oven at 110 °C and allowed to cool slowly to room temperature at a rate of 3 °C h^{-1}, whereupon metallic black square- or rectangle-shaped crystals started to form. The crystals were isolated by vacuum filtration and dried in an Ar-filled vacuum chamber at room temperature.

$(BA)_2(MA)_2Pb_3I_{10}$ ($n = 3$). PbO (0.59 M), BAI (0.19 M) and MAI (0.40 M) precursors were dispersed in a concentrated HI and H_3PO_2 mixture (9:1, vol/vol) in an Ar-filled glove box, and heated at 110 °C with stirring for 40 min to give a clear yellow solution. The subsequent steps to obtain dark brown crystals were carried out in a similar way to that described in the previous section.

$(BA)_2MAPb_2I_7$ ($n = 2$). PbO (0.59 M), BAI (0.43 M) and MAI (0.31 M) precursors were dissolved in a concentrated HI and H_3PO_2 mixture (9:1, vol/vol) in an Ar-filled glove box. The subsequent steps to obtain the dark red crystals were carried out in a similar way as already described.

$(BA)_2PbI_4$ ($n = 1$). PbO (0.57 M) and BAI (0.57 M) precursors were dissolved in a concentrated HI and H_3PO_2 mixture (10:1, vol/vol) in an Ar-filled glove box. Subsequent steps to obtain the orange crystals were carried out in a similar way as described already.

Calculation of figures of merit for 2D perovskite photodetector. *On light/off light current ratio.* The RPP perovskite devices exhibit extremely low dark current ($\sim 1 \times 10^{-13}$ A) due to its rather insulating nature in the dark, which is the key factor for the high sensitivity of the photodetector. Under illumination, photocurrent increases linearly with incident power. At 346 μW incident power, the devices display on/off current ratios of more than 10^5 (Fig. 3d) and 10^6 (Fig. 3e) for exfoliated monolayer and bulk 2D perovskite flakes, respectively.

Responsivity. Responsivity (R) is the ratio between the photocurrent (I_{ph}) and the total incident optical power (P_{in}) on the device: $R = I_{ph}/P_{in}$, so R is a function of the incident light power. To record spatially precise photocurrent on atomically thin 2D perovskite flake, a focused laser was used as the illumination source to ensure that the area irradiated was continuous and of uniform thickness. The size of the focused laser spot was ~ 1 μm^2, and the maximum responsivities of 11.3, 25 and 71.9 mA W^{-1} were achieved at 36 nW incident power for a monolayer in a relaxed state, bilayer and bulk flakes, with photocurrents of 0.41, 0.87 and 2.6 nA, respectively. To assess the performance of the bulk 2D perovskite, the photocurrents were excited using both focused and defocused lasers. It should be noted that the calculation of R using defocused laser illumination generally gives much higher values than a focused laser for the same device. For example, based on a defocused laser spot of ~ 4 mm and an active working area of 4 μm^2 for our device, the light power received by the device is calculated to be 6.36×10^{-6} nW at 20 nW incident power[28]. Thus, a high responsivity of 7.43×10^4 A W^{-1} was calculated for bulk 2D perovskite flake with a detected photocurrent of 4.37×10^{-10} A under 3.5 V (Supplementary Fig. 10j).

IQE. The definition of IQE is the number of measured charge carriers n_e divided by the number of absorbed photons n_{photon}^{abs}. After accounting for photon losses due to transmission, we can determine the amount of absorbed photons (Supplementary Fig. 10a–g) and calculate the IQE. The light absorptions of monolayer, bilayer and bulk RPP flakes exfoliated on quartz substrate were determined to be 8, 13 and 85% at 532 nm, respectively. Therefore, the calculated IQE values are 34% and 44% for monolayer and bilayer 2D perovskite photodetector, respectively.

Detectivity D^*. The detectivity (D^*) is another figure of merit for photodetectors, and is related to the sensitivity with which a detector can distinguish from background noise. It is defined as $D^* = (Af)^{1/2}/NEP$ where A is the area of the photodetector and NEP is the noise equivalent power. NEP includes flicker noise, Johnson noise and shot noise. Usually, the main contributor of NEP is shot noise P (ref. [29]). When calculating the detectivities of our monolayer and bilayer devices, an area of 1 μm^2 (focus laser spot) was selected under focus laser illumination (this is the lower bound limit). The detectivities of our monolayer and bilayer devices were calculated to be 4.7×10^{10} and 1.02×10^{11} Jones, respectively. The areas of the bulk devices were calculated to be 22.5 μm^2 (Supplementary Fig. 10i) for the focused laser and 4 μm^2 for the defocused laser (Supplementary Fig. 10j), so the detectivities of the bulk device under focus and defocus laser were calculated to be 1.2×10^{12} and 1.2×10^{15} Jones, respectively.

Photoconductive gain G. The photogain can be calculated by the formula $G = (I_{ph}/P_{abs})(h\nu/q)$, where P_{abs} is the absorbed power and $h\nu$ is the photon energy[30]. A high G value means a long photocarrier lifetime combined with short carrier transit time. The photogain decreases with laser power intensity and we chose a low laser input power to maximize the gain. The laser power (P_{abs}) received by our bulk device was 6.36×10^{-6} nW at 20 nW incident power, with I_{ph} of 4.73×10^{-10} A under this power, so the calculated G was 1.73×10^5.

Photocurrent measurements. A Keithley model 6430 sub-femtoamp sourcemeter with pre-amplifier was used to measure photo and dark I–V curves from perovskite photodetector devices. The measurements were carried out at 77 K in a Janis optical cryostat chamber at high vacuum ($\sim 1 \times 10^{-5}$ torr). IPCE was measured under broadband supercontinuum laser illumination (Fianium SC-400-4) filtered for a specific wavelength by a Bragg tunable monochromator (Photon etc.). The laser beam was chopped at 347 Hz, and a lock-in amplifier (SR830) was used to detect the IPCE response sourced by 50 mV bias voltage.

AFM measurements. Monolayer RPP sheets ($n = 1$ to 4) exfoliated on a Si/SiO$_2$ substrate were measured using a Bruker Multimode 8 peak force mode AFM machine placed in a glove box.

X-ray diffraction measurements. Single-crystal X-ray diffraction measurements of bulk RPP crystals ($n = 1$ to 4) were carried out using a four circles goniometer (Bruker AXS D8 Venture) equipped with a Photon 100 CMOS active pixel sensor detector. Molybdenum monochromatized ($\lambda = 0.71073$ Å) X-ray radiation was used for the measurements. Frames were integrated with Bruker SAINT software using a narrow-frame algorithm. For example, a colourless plate of $(BA)_2PbBr_4$ ($n = 1$) with dimensions of $0.188 \times 0.158 \times 0.026$ mm^3 was mounted on fibre glass using superglue and measured at 100 K. Data were corrected for absorption effects using the multi-scan method (SADABS). The structures were solved in the orthorhombic centred unit cell and refined using SHELXT, version 2014/5 Software. Refinement of the structure was carried out by least-squares procedures on weighted F^2 values using SHELXL-2014/7 (included in the APEX3 v2016, 9.0, AXS Bruker program)[31].

Q-plus AFM measurement. nc-AFM measurements were performed under ultrahigh-vacuum conditions at 5 K using a commercial Omicron LT STM/AFM system. All topography AFM images were collected in constant-frequency-shift mode using Q-plus sensors with resonant frequency 28.2 kHz and quality factor of 10,000.

Steady-state photoluminescence measurements. Photoluminescence measurements were performed using a 532 nm femtosecond laser pulse. The frequency of the laser was doubled from 1,064 nm laser pulses using an optical parametric oscillator (Chameleon Compact OPO, APE) pumped by a mode-locked oscillator (Chameleon Ultra II, Coherent). The laser beam was focused by a ×100 objective lens (NA = 0.90) to a diffraction-limited spot with a radius of ~360 nm. The photoluminescence signals were collected in reflection geometry with an inverted microscope (Nikon Eclipse Ti). Emission from the 2D sheets was collected with the same objective lens and routed via a bundled optical fibre to a monochromator (Acton, Spectra Pro 2300i) coupled with a charge-coupled device (Princeton Instruments, Pixis 100). No sample damage was observed during the measurements.

Time-resolved photoluminescence measurements. Time-resolved photoluminescence was measured using a photon-counting photomultiplier (PMT) (PicoQuant, PMA 182), and the signals were processed using PicoHarp 300.

Confocal micro-photoluminescence measurement using a tungsten-halogen lamp. Time-dependent photoluminescence measurements were conducted using a 532 nm continuum-wavelength laser focused by a ×50 microscope objective lens (NT-MDT), with a neutral density filter to tune the laser power density. The spot size of the laser was ~1 μm. Monolayer samples were protected with a thin flake of BN, and photoluminescence signals were collected both in air and in a nitrogen-cooled Janis cryostat vacuum chamber(10^{-5}–10^{-6} torr).

Computational method. First-principles calculations were performed with density functional theory (DFT) using VASP[32]. The generalized gradient approximation (GGA) in the Perdew–Burke–Ernzerhof (PBE) format[24,33] and the projector-augmented wave (PAW) method[34] were used in all calculations. A plane wave basis with cutoff energy of 450 eV was used for all calculations. The convergence criterion for structural relaxations was set to 0.01 eV Å^{-1}. Effects of van der Waals force (through DFT + D2)[35] and spin–orbital coupling (SOC) were also considered. It had been found that for the systems under study, DFT + D2 basically agreed with DFT, and SOC dramatically reduced the bandgap of 2D monolayers, leading to much bigger errors when compared with experiments.

Data availability

The data supporting the findings of this study are available within the Article and its Supplementary Information or from the authors.

References

28. Tan, Z. J. et al. Two-dimensional (C$_4$H$_9$NH$_3$)$_2$PbBr$_4$ perovskite crystals for high-performance photodetector. *J. Am. Chem. Soc.* **138**, 16612–16615 (2016).

29. Dou, L. et al. Solution-processed hybrid perovskite photodetectors with high detectivity. *Nat. Commun.* **5**, 5404 (2014).

30. Guo, Q. S. et al. Black phosphorus mid-infrared photodetectors with high gain. *Nano. Lett.* **16**, 4648–4655 (2016).

31. Sheldrick, G. M. Crystal structure refinement with SHELXL. *Acta Crystallogr. Section C* **71**, 3–8 (2015).

32. Kresse, G. & Furthmüller, J. Efficient iterative schemes for ab initio total-energy calculations using a plane-wave basis set. *Phys. Rev. B* **54**, 11169–11186 (1996).

33. Perdew, J. P. et al. Atoms, molecules, solids, and surfaces: applications of the generalized gradient approximation for exchange and correlation. *Phys. Rev. B* **46**, 6671–6687 (1992).

34. Blöchl, P. E., Jepsen, O. & Andersen, O. K. Improved tetrahedron method for Brillouin-zone integrations. *Phys. Rev. B* **49**, 16223–16233 (1994).

35. Grimme, S. Semiempirical GGA-type density functional constructed with a long-range dispersion correction. *J. Comput. Chem.* **27**, 1787–1799 (2006).